LASER
& PHOTONICS
REVIEWS

www.lpr-journal.org

Kirigami-Inspired Reconfigurable Thermal Mimetic Device

Hang Wei, Jinxin Gu, Feifei Ren, Chenchen Geng, Huan Guan, Shuhui Liang, Qingpu Fan, Jiupeng Zhao, Chengyu Wang, Shuliang Dou, and Yao Li**

Mimicry, a biological phenomenon whereby organisms can change their morphological characteristics to resemble another object, has stimulated the unprecedented development of devices that allow the manipulation of thermal emission. Herein, inspired by biological mimicry and the pattern evolution of Chinese Kirigami, this study demonstrates a universal and effective method to prepare devices that exhibit a reconfigurable and multilevel evolution of infrared (IR) thermal images based on vanadium dioxide (VO_2). The significant discrepancy between the phase transition temperatures of VO_2 with different tungsten doping fractions affords the reconfigurable response in thermal images to varying environmental temperatures. Particularly, the large degree of freedom afforded by evolution steps and local IR emissivity further consummates the thermal mimicry ability for diverse demands. Furthermore, the ultrafast response time, notable observation angle independence, and the active control system are also demonstrated. This study offers a new perspective for reconfigurable thermal mimetic devices and provides a new path for distinct applications such as IR communication, information encryption, and virtual/augmented reality.

1. Introduction

According to the Stefan–Boltzmann law, thermal emission is ubiquitous and related to the surface temperature (T) and emissivity (ϵ) of objects.[1] It acts as convert information carriers for the temperature distribution and chemical compositions. Therefore, its manipulation and detection become critical and inspire considerable innovations, especially in thermal camouflage.[2–7]

As one of the methods of thermal camouflage, thermal stealth is to keep the objects' thermal emission consistent with the background and therefore hide the objects under IR detection, which has been widely studied.[8–11] Thermal mimicry, as the other method, which aims at emitting deceptive IR signals to mimic another object and finally misleads the IR detector, still needs further investigation.[12] Moreover, most thermal camouflage devices only serve in specific environments.[13–15] The mismatch of thermal signals happening when the background changes makes the camouflage deactivating finally. In this case, a reconfigurable thermal mimetic device for which the IR signals can be modulated in response to changing backgrounds in real time is in great demand.

To date, thermal metamaterials[5,12,16] and smart materials[17,18] are the two primary approaches to constructing reconfigurable IR patterns. However, the complex design requirements and high-cost fabrication of thermal metamaterials limit its commercial applicability. Smart materials which can change their thermal emission in response to external stimulations, including vanadium dioxide (VO_2),[19] Ge-Sb-Te alloys,[20,21] polymeric phase-change materials,[4] graphene,[22–24] and polyaniline,[25] have drawn increasing attention in recent years. Zhao et al.[4] exploited a digital light exposure method to realize the control of a polymer network formation. The distinctive crystallization behaviors of the polymer network regions caused by their different exposure times led to the dynamic vicissitude of the thermal images within dozens of seconds. Li et al.[26] realized the spatial control of the intermediate states of VO_2 in the phase transition hysteresis by regulating the light-induced heating effect generated with a laser writing system, which finally enabled the spatially resolved control of the thermal emission. However, a universal method to fabricate a device that could exhibit a dynamically reconfigurable and fast-switching evolution of thermal images without additional energy input is yet to be reported.

In this work, inspired by the stepwise fabrication process of Chinese Kirigami, we develop a dynamically reconfigurable thermal mimetic device based on patterned tungsten-doped VO_2 films with different phase transition temperatures, which exhibits a dynamic and reconfigurable thermal images evolution in response to temperatures. It is worth mentioning that, the completely modifiable dynamic evolution, including the step numbers of the multilevel process, characteristic IR images, and local IR emissivity, makes the thermal mimetic device competent for diverse demands. The phase transition under femtosecond and picosecond timescales enables the device to undergo fast-

---

H. Wei, F. Ren, C. Geng, H. Guan, Q. Fan, S. Dou, Y. Li
Center for Composite Materials and Structure
Harbin Institute of Technology
Harbin 150001, China
E-mail: dousl@hit.edu.cn; yaoli@hit.edu.cn

J. Gu, S. Liang, J. Zhao
School of Chemical Engineering and Technology
Harbin Institute of Technology
Harbin 150001, China

C. Wang
Material and Engineering College
Northeast Forestry University
Harbin 100040, China

The ORCID identification number(s) for the author(s) of this article can be found under https://doi.org/10.1002/lpor.202200383

DOI: 10.1002/lpor.202200383

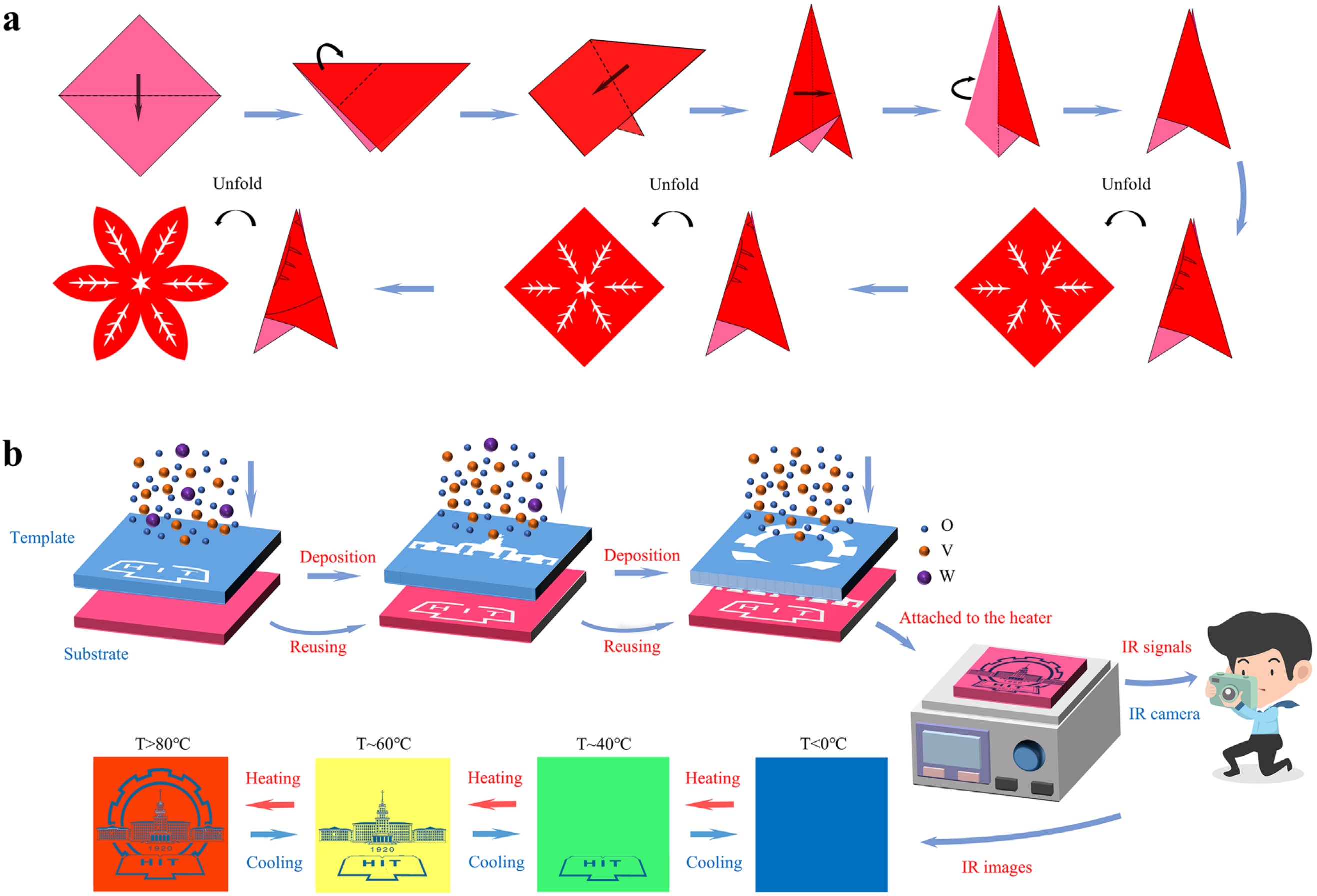

Figure 1. Schematic for the a) general fabrication method for Chinese Kirigami and b) the fabrication process for the device inspired by Kirigami and corresponding IR patterns at different temperatures.

switching. It is strongly believed that the strategy will expand the application scope for thermal mimicry, and provides potential implications for IR communication, information encryption, and AR/VR applications.

2. Results and Discussion

VO_2, a representative thermochromic material exhibiting a reversible phase transition at ≈68 °C and drastic optical changes in the IR region, is selected as the model for this study. Given the prominent lowering effect of tungsten doping on the transition temperature of VO_2,[27] and the inspiration from the dynamic evolution of patterns occurs in Chinese Kirigami owing to the stepwise approach (**Figure 1**a), we first develop a template-assisted fabrication method to realize the reconfigurable and dynamic evolution of thermal images.

As illustrated in Figure 1b, the university badge of Harbin Institute of Technology is chosen as the pattern and divided into three parts: a gear, a main building and a book. VO_2 films with tungsten doping concentrations of 0, 0.5, and 1 at% labeled W0-VO_2, W1/2-VO_2, and W1-VO_2, are deposited on the SiO_2 substrate using templates to form patterns of the gear, building and book, respectively. Consequently, the patterns are exposed in sequence when the temperature rises and finally, exhibit a dynamic evolution of thermal images due to different phase transition temperatures of the VO_2 films derived from various tungsten doping concentrations.

The VO_2 films are fabricated according to the Experimental Section, and the physical properties are investigated by scanning electron microscopy (SEM), atomic force microscopy (AFM), X-ray photoelectron spectroscopy (XPS), X-ray diffraction (XRD), and Raman spectra in Figures S1 and S2 (Supporting Information). It is apparent that the prepared VO_2 films are homogeneous and sufficiently pure for subsequent experiments. To verify the feasibility of the thermal mimetic device, a device with a two-step dynamic evolution of thermal images is prepared. The patterns of the gear and building are constructed by W0-VO_2 and W1-VO_2 films, respectively. The observed evolution of the device is shown in **Figure 2**a and Movie S1 (Supporting Information).

Temperature-dependent IR reflectance spectra of the two VO_2 films are shown in Figure 2b–e. The reflectance ranging from 7.5 to 14 μm can be used to explain the dynamic evolution. At 20 °C, both patterns are disguised due to the negligible emissivity difference compared to the substrate. With increasing temperature, the main building pattern composed of the W1-VO_2 film appears first and becomes clearly visible at 40 °C due to its lower phase transition temperature. Upon further heating, the gear composed of

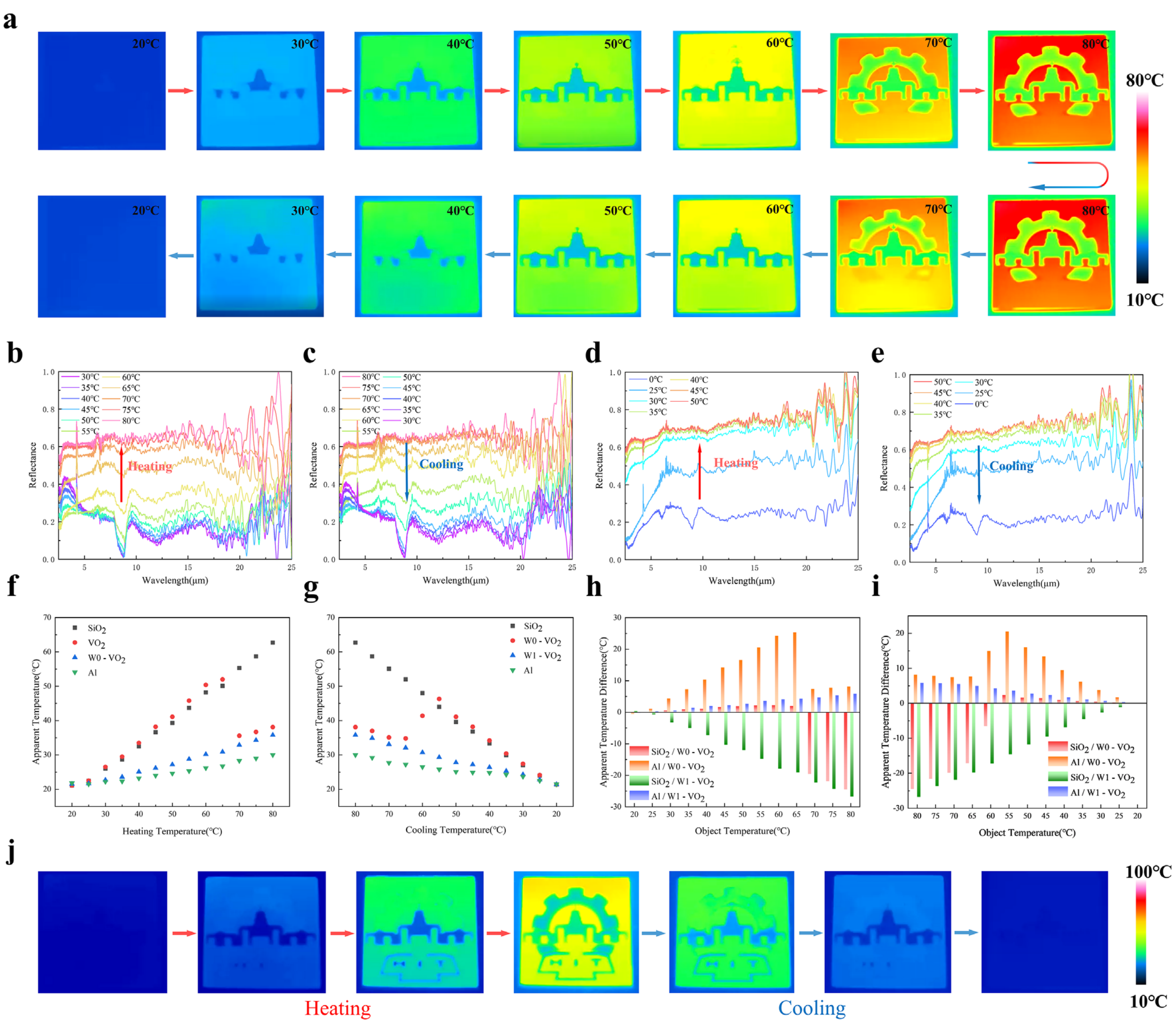

Figure 2. a) Evolution of IR images of the device upon heating and cooling process. The temperature in the upper right corner represents the actual temperature. Temperature-dependent IR reflectance spectra of b,c) W0-VO_2 film and d,e) W1-VO_2 film during heating and cooling. f,g) Apparent temperatures of the SiO_2 substrate, W0-VO_2 film, W1-VO_2 film, and Al bowl during heating and cooling. h,i) Apparent temperature differences during heating and cooling. j) IR image evolution of the device exhibiting the multilevel control capability.

the W0-VO_2 film emerges at 70 °C, and is completely exposed at 80 °C. During the cooling process, the gear and the main building disappear in reverse order, and the patterns are completely concealed after the temperature reaches 20 °C.

To further understand the reversible evolution process of the device, the apparent temperatures of the SiO_2 substrate, the main building, the gear, and an aluminum (Al) plate are recorded by the IR camera, respectively (Figure 2f,g). The SiO_2 substrate and Al plate can help determine whether the pattern is low emissivity or high emissivity intuitively (Figure S3, Supporting Information).

The radiation of objects can be calculated according to the Stefan–Boltzmann law. The received radiation consists of the actual radiation emitted from the object, surroundings, atmosphere, and the compensation inside the IR camera [Equations (1)–(4)][28]

$$P_A = \tau P_R + (1 - \tau)\, P_{atm} + \tau P_{ref} + P_{com} \tag{1}$$

$$P_R = \varepsilon_R \sigma T_R{}^4 \tag{2}$$

$$P_A = \varepsilon_A \sigma T_A{}^4 \tag{3}$$

$$P_{ref} = (1 - \varepsilon)\, P_{sur} \tag{4}$$

where $P_{R/A}$ represents the radiation from the object and the received radiation of the IR camera, P_{atm} represents the radiation from the atmosphere, P_{ref} represents the radiation from the surroundings, P_{com} represents the compensation inside the IR camera. τ represents the atmospheric transmission, $\epsilon_{\mathrm{R/A}}$ represents the real and apparent emissivity, $T_{\mathrm{R/A}}$ represents the real and apparent temperatures, and σ is the Stefan–Boltzmann constant. Herein, it is worth noting that the measured IR wavelength is 7.5–14 μm, which is highly transmissive, so that τ is set to 1. Meanwhile, ϵ_{A} here is set to 1 inside the IR camera. Therefore, the relationship between the apparent temperature and the actual surface emissivity is described in Equation (5)

$$T_{\mathrm{A}} = T_{\mathrm{R}}\sqrt[4]{\frac{\varepsilon_{\mathrm{R}}}{\varepsilon_{\mathrm{A}}} - \frac{P_{\mathrm{ref}} + P_{\mathrm{com}}}{T_{\mathrm{R}}}} \tag{5}$$

Then, the apparent temperature T_{A} can be regarded as an index that reflects the emissivity at a certain temperature T_{R}. Therefore, the apparent IR signals of patterns with low emissivity are similar to that of Al, whereas similar to that of the $\mathrm{SiO_2}$ substrate when the patterns exhibit high emissivity. In Figure 2h,i, the differences in apparent temperatures between the patterns and substrates are recorded. Initially, it is clear that negligible apparent temperature differences between the patterns and $\mathrm{SiO_2}$ (red and green columns) make both patterns hidden in the environment. Once it is heated, the apparent temperatures of $\mathrm{SiO_2}$ and Al increase linearly according to Equation (5). However, the apparent temperature of the W1-$\mathrm{VO_2}$ film undergoes a period of minimal change due to the inverse change trend of T_{R} and ϵ_{R}. Therefore, the steadily increasing apparent temperature difference between W1-$\mathrm{VO_2}$ and $\mathrm{SiO_2}$ allows the main building to manifest. Meanwhile, as the difference between W0-$\mathrm{VO_2}$ and $\mathrm{SiO_2}$ maintains around 0, the gear remains invisible. When the temperature exceeds 70 °C which is higher than the phase transition temperature of W0-$\mathrm{VO_2}$, the gear is exposed due to the significant change in the apparent temperature difference with the $\mathrm{SiO_2}$ substrate. Finally, after the temperature of device reaches 80 °C, both the phase transition processes are complete, and the patterns reveal distinct color difference relative to the $\mathrm{SiO_2}$ substrate.

Upon cooling, the IR images undergo a fully reversible evolution. The gear disappears at around 60 °C and the main building disappears at ≈20 °C. Herein, the hysteresis effect, especially for W0-$\mathrm{VO_2}$ should be noted. A reconfigurable thermal mimetic device based on patterned tungsten-doped $\mathrm{VO_2}$ films with different phase transition temperatures is realized. The temperature-dependent IR reflectance spectra indicates that the emissivity during the cooling process is higher than that of the heating process at the same temperature (Figure 2b–e). In addition, the apparent temperature difference between W0-$\mathrm{VO_2}$ and $\mathrm{SiO_2}$ keeps negative until 55 °C, exhibiting a lag of ≈5 °C relative to the heating process, which coincides with the thermal hysteresis loops shown in Figure S4 (Supporting Information).

Based on these results, we expected that a three-step evolution could be accomplished by utilizing $\mathrm{VO_2}$ films with various doping concentrations. As shown in Figure 2j and Movie S2 (Supporting Information), the process is realized with the participation of W1/2-$\mathrm{VO_2}$. W1/2-$\mathrm{VO_2}$ is used to depict the "book" which is located at the bottom of the school badge, and manifests at ≈40 °C. Figure S5 (Supporting Information) demonstrates the temperature-dependent IR reflectance spectra. When the temperature reaches 80 °C, the entire school badge can be observed. Thus, a dynamic evolution of IR images with several steps is achieved, which means that this technology can be likely applied to more complex and diverse demands.

Herein, it is noticed that there is no spatial overlap between all patterns in Figure 2. Overlap of the patterns could be problematic if it disturbs the dynamic evolution, as larger substrates are required to avoid the overlap in multilevel and complex evolutions, which would ultimately result in increased cost and difficulty of design. To investigate the issue, we deposit W0-$\mathrm{VO_2}$ on the $\mathrm{SiO_2}$ substrate using a unicorn template and then deposit the W1/2-$\mathrm{VO_2}$ film on top of the unicorn with the assistance of a swallow template. Fortunately, the results in **Figure 3**a and Movie S3 (Supporting Information) demonstrate that the overlapping causes no problems. The swallow appears first when the device is placed on a heated plate of 100 °C, followed by the image transforming to a unicorn. Evolution in this experiment proceeds similarly to that in the earlier experiments shown in Figure 2. The success of our pattern stacking experiment indicates that it is a more convenient method to match the requirements of designing devices with more complex evolutions. In addition, another fantastic performance should be mentioned is the fast response time. Owing to the ultrafast phase transition of $\mathrm{VO_2}$ which is under femtosecond and picosecond timescales, it only takes 3 s to accomplish the whole evolution, showing significant advantages compared to reported thermal mimetic materials.[4]

In addition to the proof of feasibility, the application of thermal mimicry aiming at various environments is also considered. Biological organisms exhibit characteristic thermal signals due to their diverse emissivity. Therefore, to mimic their characteristic IR signals perfectly, the accurate thermal control of local emissivity at a certain temperature is crucial. A basic Fabry–Pérot cavity structure of $\mathrm{VO_2/HfO_2/Au}$ is used to manipulate the local IR emissivity continuously. We simulate the emissivity of our device by altering the thickness of $\mathrm{HfO_2}$ and $\mathrm{VO_2}$ respectively (Figure S6, Supporting Information). According to Equation (5), when T_{R} is fixed, the apparent temperatures T_{A} of the patterns can be predicted roughly if the radiation emitted from the surroundings P_{ref} and the compensation inside the IR camera $\mathrm{P_{com}}$ are ignored. Meanwhile, we fix the color bar to prevent it from interfering with the display. The results demonstrate that the IR signals vary from blue to red in response to specific structural parameters at ≈80 °C (Figure 3b), revealing that local IR emissivity is well-regulated using this method. To validate the method experimentally, we fix the thickness of W1/2-$\mathrm{VO_2}$ to 50 nm and vary the thicknesses of the $\mathrm{HfO_2}$ layer. As the Au layer is deposited at the bottom of the cavity, the areas not covered with $\mathrm{VO_2}$ are visualized as low emissivity using the IR camera at 80 °C. The three gears in Figure 3c reveal gradually increasing apparent temperatures with $\mathrm{HfO_2}$ thickness through an IR signal change from green to bright red. We then further design and prepare patterns with diverse IR signals, which are shown at the bottom of Figure 3c. Each part of the school badge, rainbow, and flower exhibits diverse IR colors whose actual temperatures are fixed at 100 °C, respectively. The high apparent temperatures indicate that thicker $\mathrm{HfO_2}$ layers are deposited in these areas. Therefore, we have successfully demonstrated the potential in the accurate local emissivity control and confirmed the endless possibilities for thermal mimicry.

The observing angles independence of the device is tested in Figure 3d. We prepare a "World Cup" pattern for the test. The

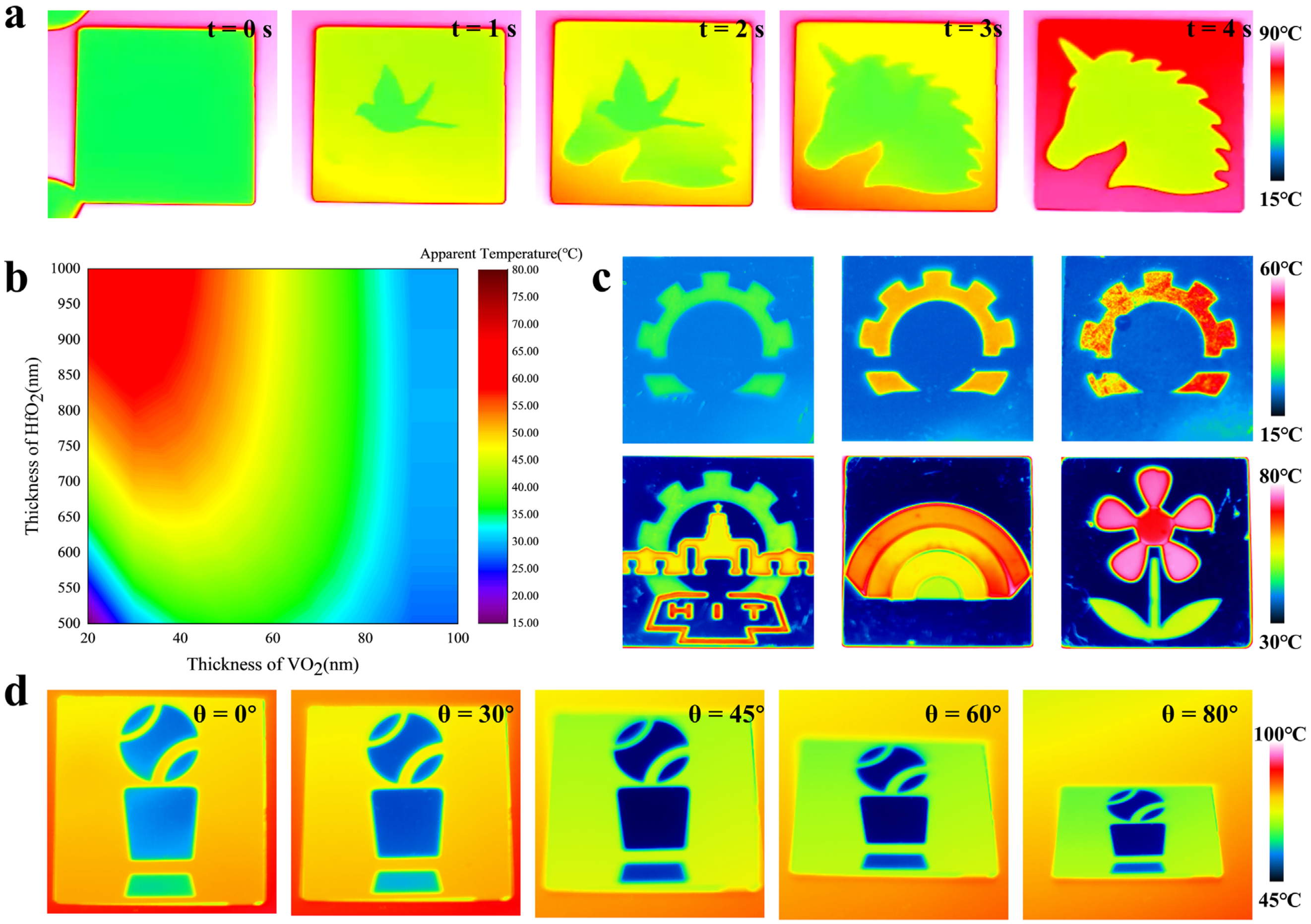

Figure 3. a) Illustration of the evolution of overlapping patterns. b) Colors captured by the IR camera corresponding to different parameters at 80 °C, and fixed color bar. c) Illustration of different IR signals in response to different thicknesses of HfO_2. d) IR images of "World Cup" under different observing angles ($\theta = 0°$, 30°, 45°, 60°, and 80°).

"World Cup" is clearly distinguishable under a series of observing angles of 0°, 30°, 45°, 60°, and 80°, which indicates the outstanding observing angles independence. Finally, we add an indium tin oxide conductive layer as the active joule-heating control unit on the back of the device. The active control unit functions as a self-contained system to compensate for the inadequacy of the environmental temperature to induce the appearance of the corresponding infrared patterns (Figure S7 and Movie S4, Supporting Information). These results confirm and promote the safety and controllability of the thermal mimetic device.

3. Conclusion

In summary, we demonstrate, for the first time, a simple but highly effective method to design reconfigurable thermal mimetic devices based on VO_2. The large disparity in transition temperatures of VO_2 with different W doping levels affords a multilevel reconfigurable response of thermal images to dynamic environmental temperatures. A stacking method is proposed to overcome the spatial constraints for a more complex thermal mimicry process. The large degree of freedom in the local IR emissivity and patterns, together with the evolution steps, demonstrates that the thermal mimetic ability can be tailored to meet diverse requirements. Furthermore, the technology is highly practicable because of the ultrafast response time, prominent observing angle independence (up to ≈80°) and the active control system. We believe our strategy opens up new avenues for thermal camouflage, and will inspire expansive applications including communication, information encryption, and AR/VR applications.

4. Experimental Section

Materials: Three vanadium targets with different tungsten doped levels of 0, 0.5, and 1 at%, gold and hafnium targets with purity of 99.9% and diameter of 76.2 mm were purchased from ZhongNuo Advanced Material (Beijing) Technology Co., Ltd. Argon (Ar) and oxygen (O_2) used in experiments were both of 99.9995% purity and purchased from Liming Gas Group Co., Ltd. SiO_2 substrates (4×4 cm^2) were all cleaned using deionized (DI) water and alcohol and dried by a stream of pure nitrogen (N_2).

Films Preparation: The high-power pulsed magnetron sputtering system (MS650C) was purchased from KeYou, China. All VO_2 films were fabricated by the high-power pulsed magnetron sputtering while Au and HfO_2 layers were fabricated by the DC magnetron sputtering.

Preparation of Devices in Figure 2: First of all, corresponding templates were attached to SiO_2 substrate before deposition. The SiO_2 substrate was taken from the chamber after W0-VO_2 was deposited for 75 min with the gear template, and then, the gear was replaced with the book template and continued depositing W1/2-VO_2 for 75 min. Finally, the preparation was finished when W1-VO_2 was deposited for 75 min with the main building template. During the deposition process, the Ar/O_2 ratios were fixed at 81:1.7, 81:1.9, and 81/2.0 sccm for W0-VO_2, W1/2-VO_2, and W1-VO_2, and corresponding sputtering powers were set as 180, 180, and 200 W. The chamber pressure, substrate temperature, input pulse frequency, and width were fixed at 0.9 Pa, 550 °C, 200 Hz, and 50 µs, respectively.

For Preparation of Devices in Figure 3: Au layer was firstly deposited by the gold target on SiO_2 substrate with the DC power density of 100 W and Ar flow of 81 sccm for 15 min. Then, corresponding templates were attached to prepared Au/SiO_2 substrates, and HfO_2 and VO_2 layers were deposited in steps. HfO_2 layer was deposited by the hafnium target with the DC power density of 200 W and Ar/O_2 flow ratio of 81/4.9 sccm, whose deposition time was decided according to diverse designs. The deposition of VO_2 layers with different doping levels was the same as above mentioned.

Measurements: The crystalline phases were characterized using XRD (PANalytical B.V. Model Xpert Pro). The surface morphologies and thickness were evaluated by an AFM (Dimension Icon, Bruker) and a field emission scanning electron microscope (FEI Helios Nanolab600i). Fourier transform infrared (FTIR) spectroscopy was performed using an FTIR system (VERTEX-70, Bruker) from 2.5 to 25 μm, to measure the reflectance spectrum. XPS was performed with a PHI 5700 ESCA System using Al Ka radiation (1486.6 eV). XPS data were calibrated to the C1s peak and analyzed using Casa XPS software. The IR images were recorded by thermal imager (TIX-660, FLUKE) from 7.5 to 14 μm.

Supporting Information

Supporting Information is available from the Wiley Online Library or from the author.

Acknowledgements

The authors thank the National Natural Science Foundation of China (51902073), China Postdoctoral Science Foundation Funded Project (2019M661273, 2020T130142), Heilongjiang Province Postdoctoral Science Foundation (LBH-Z19159), and the Fundamental Research Funds for the Central Universities (HIT.NSRIF.2020019, Grant No. HIT.OCEF.2021004, FRFCU5710090220).

Conflict of Interest

The authors declare no conflict of interest.

Data Availability Statement

Research data are not shared.

Keywords

designability, reconfigurable, thermal mimicry, VO_2

Received: May 27, 2022
Revised: July 20, 2022
Published online:

---

[1] X. Liu, T. Tyler, T. Starr, A. F. Starr, N. M. Jokerst, W. J. Padilla, *Phys. Rev. Lett.* **2011**, *107*, 045901.
[2] J. Xu, J. Mandal, A. P. Raman, *Science* **2021**, *372*, 393.
[3] D. G. Baranov, Y. Xiao, I. A. Nechepurenko, A. Krasnok, A. Alu, M. A. Kats, *Nat. Mater.* **2019**, *18*, 920.
[4] S. Deng, L. Huang, J. Wu, P. Pan, Q. Zhao, T. Xie, *Adv. Mater.* **2021**, *33*, 2008119.
[5] Z. Xu, H. Luo, H. Zhu, Y. Hong, W. Shen, J. Ding, S. Kaur, P. Ghosh, M. Qiu, Q. Li, *Nano Lett.* **2021**, *21*, 5269.
[6] R. Hu, S. Zhou, Y. Li, D. Y. Lei, X. Luo, C. W. Qiu, *Adv. Mater.* **2018**, *30*, 1707237.
[7] S. Hong, S. Shin, R. Chen, *Adv. Funct. Mater.* **2020**, *30*, 1909788.
[8] L. Li, M. Shi, X. Liu, X. Jin, Y. Cao, Y. Yang, W. Wang, J. Wang, *Adv. Funct. Mater.* **2021**, *31*, 2101381.
[9] Y. Cui, H. Gong, Y. Wang, D. Li, H. Bai, *Adv. Mater.* **2018**, *30*, 1706807.
[10] R. Hu, W. Xi, Y. Liu, K. Tang, J. Song, X. Luo, J. Wu, C.-W. Qiu, *Mater. Today* **2021**, *45*, 120.
[11] M. Li, D. Liu, H. Cheng, L. Peng, M. Zu, *Sci. Adv.* **2020**, *6*, eaba3494.
[12] B. Xiong, Y. Xu, J. Wang, L. Li, L. Deng, F. Cheng, R. W. Peng, M. Wang, Y. Liu, *Adv. Mater.* **2021**, *33*, 2005864.
[13] M. Pan, Y. Huang, Q. Li, H. Luo, H. Zhu, S. Kaur, M. Qiu, *Nano Energy* **2020**, *69*, 104449.
[14] H. Zhu, Q. Li, C. Tao, Y. Hong, Z. Xu, W. Shen, S. Kaur, P. Ghosh, M. Qiu, *Nat. Commun.* **2021**, *12*, 1805.
[15] Y. Huang, B. Ma, A. Pattanayak, S. Kaur, M. Qiu, Q. Li, *Laser Photonics Rev.* **2021**, *15*, 2000391.
[16] J. Du, L. Sheng, Y. Xu, Q. Chen, C. Gu, M. Li, S. X. Zhang, *Adv. Mater.* **2021**, *33*, 2008055.
[17] S. Dou, H. Xu, J. Zhao, K. Zhang, N. Li, Y. Lin, L. Pan, Y. Li, *Adv. Mater.* **2020**, *33*, 2000697.
[18] H. Wei, J. Gu, F. Ren, L. Zhang, G. Xu, B. Wang, S. Song, J. Zhao, S. Dou, Y. Li, *Small* **2021**, *17*, 2100446.
[19] K. Tang, X. Wang, K. Dong, Y. Li, J. Li, B. Sun, X. Zhang, C. Dames, C. Qiu, J. Yao, J. Wu, *Adv. Mater.* **2020**, *32*, 1907071.
[20] K. K. Du, Q. Li, Y. B. Lyu, J. C. Ding, Y. Lu, Z. Y. Cheng, M. Qiu, *Light: Sci. Appl.* **2017**, *6*, e16194.
[21] Y. Qu, Q. Li, L. Cai, M. Pan, P. Ghosh, K. Du, M. Qiu, *Light: Sci. Appl.* **2018**, *7*, 26.
[22] O. Salihoglu, H. B. Uzlu, O. Yakar, S. Aas, O. Balci, N. Kakenov, S. Balci, S. Olcum, S. Suzer, C. Kocabas, *Nano Lett.* **2018**, *18*, 4541.
[23] M. S. Ergoktas, G. Bakan, P. Steiner, C. Bartlam, Y. Malevich, E. Ozden-Yenigun, G. He, N. Karim, P. Cataldi, M. A. Bissett, I. A. Kinloch, K. S. Novoselov, C. Kocabas, *Nano Lett.* **2020**, *20*, 5346.
[24] M. S. Ergoktas, G. Bakan, E. Kovalska, L. W. Le Fevre, R. P. Fields, P. Steiner, X. Yu, O. Salihoglu, S. Balci, V. I. Fal'ko, K. Novoselov, R. A. W. Dryfe, C. Kocabas, *Nat. Photonics* **2021**, *15*, 493.
[25] G. Xu, B. Wang, S. Song, Z. Ren, J. Li, X. Xu, W. Zhou, H. Li, H. Yang, L. Zhang, Y. Li, *Chem. Eng. J.* **2021**, *422*.
[26] Z. Xu, Q. Li, K. Du, S. Long, Y. Yang, X. Cao, H. Luo, H. Zhu, P. Ghosh, W. Shen, M. Qiu, *Laser Photonics Rev.* **2019**, *14*.
[27] Y. Cui, Y. Ke, C. Liu, Z. Chen, N. Wang, L. Zhang, Y. Zhou, S. Wang, Y. Gao, Y. Long, *Joule* **2018**, *2*, 1707.
[28] T. Hamrelius, *Thermosense XIII* **1991**, *1467*, 448.